Spatial response of infrared antennas

C. Fumeaux [a], G.D. Boreman [b], W. Herrmann [a], H. Rothuizen [b], F.K. Kneubühl [a]

[a] Institute of Quantum Electronics, Swiss Federal Institute of Technology (ETH), CH-8093 Zürich, Switzerland

[b] Center for Research & Education in Optics & Lasers (CREOL), University of Central Florida, Orlando, FL 32816-2700 USA

[c] IBM Research Laboratory, Säumerstrasse 4, CH-8803 Rüschlikon, Switzerland

ABSTRACT

We present measurements on the spatial-response profiles of nanometer-scale thin-film Ni-NiO-Ni diodes integrated with infrared dipole and bow-tie antennas. Antennas are usually tested for their angular response using collimated radiation. However, in this study, focused radiation with a wavelength of 10.6 μm is scanned across the receiving area of the detector. This permits determination of the effective collection area of an individual infrared antenna. The width of the collection area parallel to the antenna axis is shown to scale with the physical length of the antenna. The determination of the effective collection area permits a characterization of the fringe fields surrounding the antenna and can be used to investigate the cross talk between adjacent antennas. It allows calculation on the power collected by an infrared antenna for a given irradiance of the illuminating beam. The spatial response also gives insight into the current-wave modes propagating on the antenna.

Keywords: infrared antenna, impulse response, MOM diodes

Fast infrared detectors have dimensions considerably smaller than the wavelength of the incident radiation. Their performance is enhanced with the aid of wire or planar antennas having dimensions comparable with the wavelength. The efficiency of infrared lithographic antennas for detection at wavelengths near 10 μm was demonstrated with various types of detectors, including thin-film metal-oxide-metal diodes (MOM or MIM) [1-5] and Nb microbolometers[6]. To investigate the mechanism of infrared antennas, we determine the spatial response of various dipole and bow-tie antennas at 10.6 μm wavelength. For this purpose, we scan tightly focused radiation at normal incidence across the receiving area of the detector in two orthogonal directions.

The effective receiving area is a relevant parameter for infrared antennas. It first permits a radiometric characterization of the detector based on received power for a given incident irradiance. It also defines the spacing of individual detectors required for construction of an area receiver, and in a two-dimensional array allows calculation of cross-talk level between adjacent devices.[7,8] The spatial response of infrared antennas on a substrate also contributes to the understanding of the resonant modes propagating on the structure.

1. THIN-FILM ANTENNA-COUPLED MOM DIODES

Detection with point-contact MOM diodes at a wavelength of 10.6 μm was first reported in 1968.[9] The mechanical instability of the point-contact configuration and the impossibility to cluster whiskers as arrays initiated the manufacture of thin-film MOM diodes integrated with infrared antennas.[1,2,10] We have also reported on our own development of thin-film Ni-NiO-Ni diodes and their application as detectors and mixers for 30 THz CO_2-laser radiation.[2-5, 11-14] These papers present the analysis of these diodes with a minimal contact area of approximately 110 nm × 110 nm connected to dipole, bow-tie and spiral antennas. The fabrication of the nanometer-scale diodes on a silicon substrate is described in detail in Ref. [4]. The small contact structures necessary for a fast diode response are defined with direct-writing electron-beam lithography at the IBM Research Laboratory, Rüschlikon. Figure 1 shows a schematic cross section of the diode and indicates the different layer thicknesses. Our diodes are manufactured on 385 μm silicon substrates coated on both sides with 1.5 μm silicon-dioxide layers. These two SiO_2 layers act as antireflection coating and yield a 78% transmission of infrared radiation at the wavelength of 10.6 μm (28 THz) through the three-layer substrate.

Further author information -
C.F. (correspondence): c/o G.D. Boreman, CREOL, University of Central FLorida, Orlando, FL 32816-2700 USA
G.D.B.: Email: boreman@lorien.creol.ucf.edu; Telephone: 407-823-6815

Part of the SPIE Conference on Infrared Detectors and Focal Plane Arrays V • Orlando, Florida • April 1998
SPIE Vol. 3379 • 0277-786X/98/$10.00

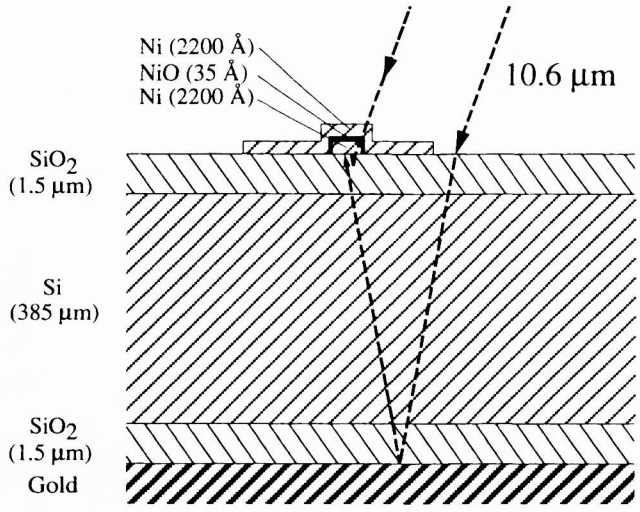

Fig. 1: Schematic cross section of our Ni-NiO-Ni diode.

The diode is irradiated from the air side. A gold mirror at the back side of the chip reflects the incident radiation to the diode and its antenna (Fig. 1). This permits to take advantage of the better sensitivity of the antenna to radiation incident from the substrate side.[15]

The effective wavelength λ_{eff} of the currents propagating in our antennas is determined by the effective relative electric permittivity ε_{eff} of a structure. At the applied frequency of 28 THz, the effective wavelength can be approximated by the wavelength in the silicon substrate $\lambda_{eff} \approx \lambda_{subst} \approx 3.1$ μm.[14] We have measured the spatial response of a full-wave dipole antenna (Fig. 2) and of bow-tie antennas (Fig. 3) with three different half arm lengths L/2 = 1.9 μm, 2.3 μm and 3.9 μm. The full-wave dipole has a length L that corresponds to the effective wavelength $L \approx \lambda_{eff} \approx 3.1$ μm.[3] The shortest bow-tie length corresponds to the third resonance of the impedance measured by Brown & Woodward [16] for a triangular unipole in free-space. The two longer bow-tie arms correspond to the resonant full lengths L equal 3/2 and 5/2 the effective wavelength λ_{eff} of our 28 THz laser radiation.[17]

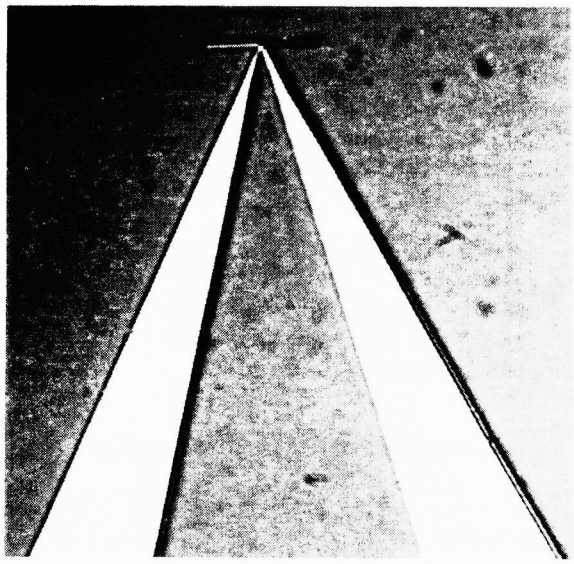

Fig. 2: Photograph of our thin-film Ni-NiO-Ni diode with integrated dipole antenna and its connections.

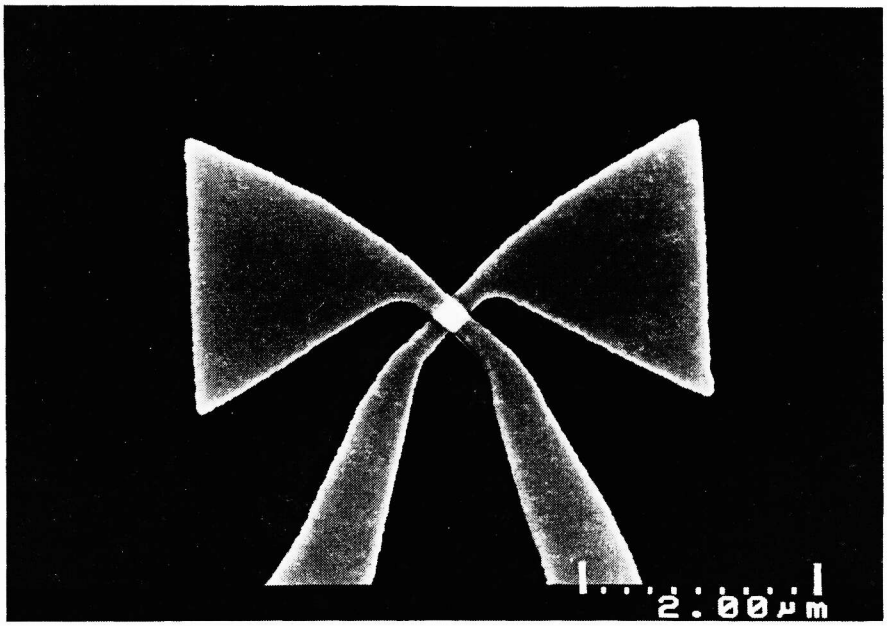

Fig. 3: Electron microscope image of our thin-film Ni-NiO-Ni diode with integrated bow-tie antenna with a flare angle of 60° and with a half arm-length L/2 = 2.3 µm.

The Ni-NiO-Ni diodes used for the experiments described here have contact areas of approximately 180 nm × 180 nm. These contact areas are larger than our minimal contact areas. As a consequence, these diodes exhibit smaller responses but high-power damage thresholds.

The detection mechanism with our thin-film MOM diodes includes several additive effects.[18] The principal mechanism of rectification of ac antenna currents is nonlinear electron tunneling through an extremely thin oxide layer. In our thin-film Ni-NiO-Ni diodes, another significant contribution to the detection signal is of thermal origin: The absorption of radiation in the SiO_2-layer of the substrate increases the temperature of the MOM diode and therefore causes emission of thermally excited electrons over the oxide barrier. The polarization dependence of the signal permits an approximate distinction of the two contributions. The maximal signal V_{max} is measured for the polarization of the incident 28 THz radiation parallel to the antenna axis and the minimal signal V_{min} for the cross-polarization. The polarization-independent contribution V_{min} is attributed to the polarization-independent thermal effects.[4] The polarization-dependent part of the signal as a function of the polarization angle can be accurately described by a cosine squared with amplitude $\Delta V = V_{max} - V_{min}$. It can be attributed entirely to antenna coupling, which was confirmed by our mixing experiments.[12,13] At difference frequencies in the GHz range, the thermal effects are too slow to contribute to the mixing signal. We measured at 58 GHz a ratio $\Delta V/V_{min}$ of over 50 with a diode connected to a bow-tie antenna with the half-length L/2 = 2.3 µm. This demonstrates the almost perfect linear polarization response of this antenna.

The distinct nature and the additivity of thermal and antenna signals result in different spatial responses. The beam profiles of the two contributions V_{min} and ΔV measured with our antenna-coupled detectors are consequently expected to show different widths. According to antenna theory, the effective receiving area of the antenna is expected to depend on the physical antenna geometry. On the contrary, the profile of the thermal response V_{min} should exhibit a circular symmetry and moreover an area independent of the antenna type.

2. EXPERIMENTAL PROCEDURE

The diode and its antenna are mounted on an x-y-z holder manipulated by micropositioners. The diode is scanned at normal incidence through the focus of a linearly polarized CO_2-laser beam with a wavelength of 10.6 µm. The radiation in a TEM_{00} mode is focused by a well-corrected lens with a 25.4-mm focal length. This results in a nearly diffraction-limited system with a f-number between F/1 and F/2.[19] The polarization of the infrared radiation can be rotated with a CdS half-wave plate. The signal is measured with lock-in techniques.[3]

Each beam-profile measurement is performed with the diode and its antenna as illustrated in Fig. 4. First we maximize the signal by position adjustment in all three directions. The optimization of the z-location positions the antenna into the focus of the laser beam. The beam profile measured with the diode and its antenna is then recorded in one principal direction across the center of the beam with 5 μm increments. The 90° rotation of the polarization with the half-wave plate permits recording the profiles first for the polarization parallel and secondly for the polarization perpendicular to the antenna axis. The measurement of the beam profiles in the other principal direction is performed similarly for both polarizations after a 90° rotation of the antenna holder in the x-y-plane and a new adjustment to the exact beam center.

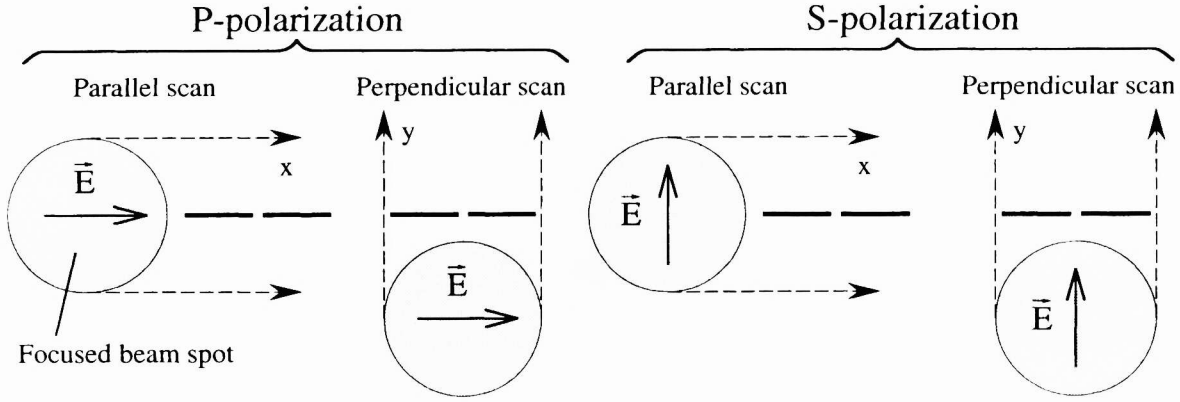

Fig. 4: General configuration of the four beam scans $V_{max}(x)$, $V_{max}(y)$, $V_{min}(x)$ and $V_{min}(y)$ performed with our antenna-coupled infrared detectors.

For each diode we consequently performed four scans as illustrated in Fig. 5. The figure shows two scans parallel to the antenna axis (parallel scans), and two scans perpendicular to the antenna axis (perpendicular scans) in both cases for P- and S- polarizations corresponding to the maximal and minimal detected voltages V_{max} and V_{min}.

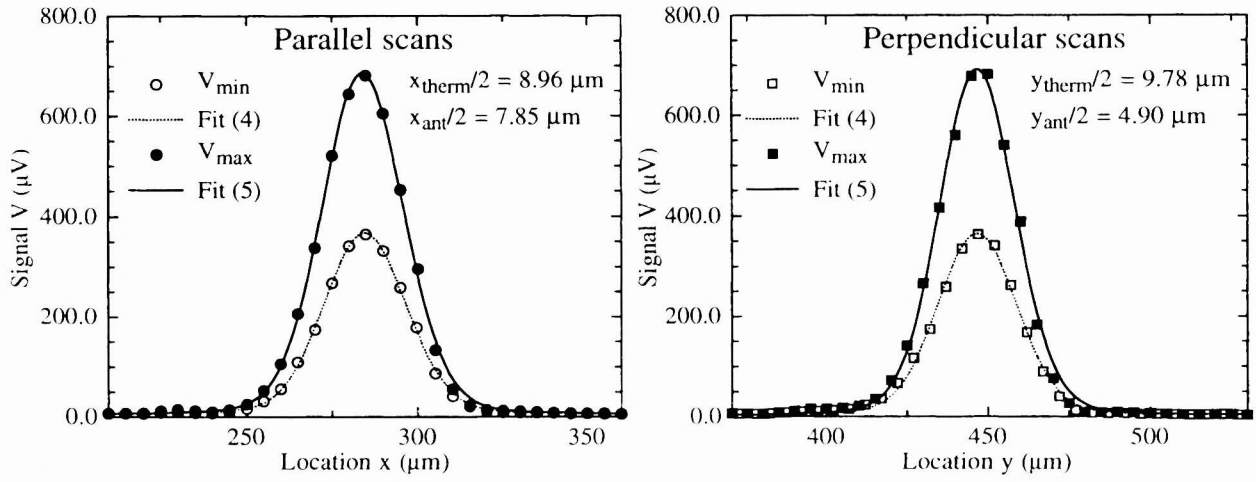

Fig. 5: Beam profiles measured with a thin-film Ni-NiO-Ni diode connected to a dipole antenna for P- and S-polarizations.

The nearly diffraction-limited Gaussian beam profile of our CO_2-laser was measured at the focus position with a knife-edge test.[20] This method yielded a $1/e^2$ minimum beam halfwidth of $w_0 = 19.54$ μm. However, this measured beam size does not correspond to the effective input beam seen by our antenna-coupled detector because of the layer structure of the supporting substrate. The beam at the location of the antenna represents the coherent addition of the beam fraction directly reflected from the first SiO_2-layer and that beam fraction reflected by the gold layer at the back side of the substrate (Fig. 1). The two beam fractions have different widths because of the tight focusing of the infrared radiation as illustrated in Fig. 6.

Constructive interference of the high-irradiance in-focus and the low-irradiance out-of-focus beams results in a slightly broadened spatial extent of the beam that illuminates the antenna. On the contrary, destructive interference narrows the input beam on the antenna.

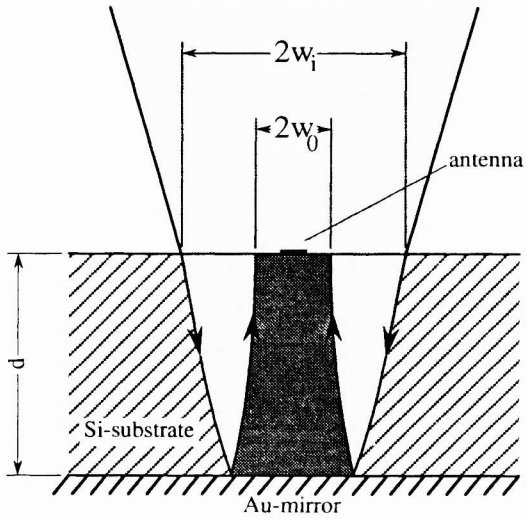

Fig. 6: Schematic showing the interference occurring at normal incidence between the fraction of the Gaussian beam reflected on the gold mirror and the fraction directly reflected on the first SiO_2-layer.

The effective beam-irradiance profile B(x) in the x-direction through the center of the beam is determined by two-beam interference according to

$$B(x) = B_1(x) + B_2(x) + 2\sqrt{B_1(x)B_2(x)}\cos\Psi_r$$

$$\text{with} \quad B_1(x) = B_0 \times \exp\left(\frac{-2(x-x_0)^2}{w_0^2}\right) \tag{1}$$

$$\text{and} \quad B_2(x) = B_0 \times \frac{P_o}{P_f} \times \exp\left(\frac{-2(x-x_0)^2}{w_i^2}\right)$$

where $B_1(x)$ and $B_2(x)$ represent the contributions of the two interfering Gaussian beams with a relative phase Ψ_r and the power ratio P_0/P_f. The location of the center of the beam is described by x_0. The radius $w_0 = 19.54$ µm of the in-focus beam corresponds to the radius at the waist of the beam measured with a knife-edge scan. We measured $w_i = 57.73$ µm for the out-of-focus beam with the knife-edge technique at the z-distance $z_d = 227$ µm from the focus in the air. This distance z_d corresponds to the reduced round-trip length in the substrate, when taking the refractive index of Si into account. The profile B(y) in the y-direction through the center of the beam is identical.

The relative phase Ψ_r depends on the substrate thickness directly under the diode. By measuring the diode response as a function of the angle of incidence θ and by subsequent fitting the results with a calculated two-beam interference function, we can determine the substrate thickness and therefore the relative phase Ψ_r between the two interfering beams. We have performed this measurement for the range of angles of incidence θ between -20° and +20° by making use of a lens with a focal length of 127 mm. A typical curve is displayed in Fig. 7. Variations of the substrate thickness are too small to be detected for the 10 diodes located on a given 3 mm × 3 mm chip so that a single phase measurement is adequate for characterization of diodes on the same chip. We determine a power ratio $P_f/P_0 \approx 4$ of the two interfering beams by a calculation that makes use of the information contained in the contrast of the interference patterns. In the data processing described in the next section, the effective irradiance beam profiles B(x) and B(y) are calculated as a function of the measured relative phase Ψ_r for each chip investigated. The detector impulse response is determined from our measured data by deconvolution.

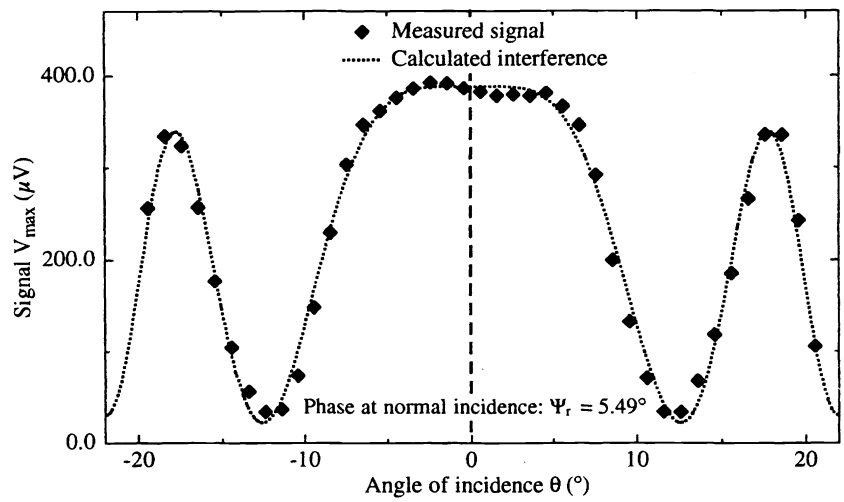

Fig. 7: Measured signal versus angle of incidence θ exhibiting an oscillation caused by substrate interference. For this measurement, the radiation with a wavelength of 10.6 μm was focused on the diode with a lens of 12.7 cm focal length.

3. DATA PROCESSING

In this study we have measured for each type of antenna investigated at least 6 complete sets of 4 scans, i.e. in x- and y-directions for S- and P-polarizations, performed with different diodes. In order to eliminate the effect of the substrate interferences described in the previous section, the diodes with the same type of antenna were located on the same chip. They showed identical interference patterns and an identical input beam.

For simplicity, we consider in the following profiles in the x-direction of an input beam centered at $x_0 = 0$ μm. The measured response of the detector $h_{meas}(x)$ in the spatial domain is the convolution of the impulse response $h_{det}(x)$ of our antenna-coupled detector and the effective beam irradiance profile B(x) described by (1) [19]

$$h_{meas}(x) = B(x) * h_{det}(x) \ . \tag{2}$$

The shape of the impulse response $h_{det}(x)$ of the detector is not known. To simplify data processing and interpretation, we assume an equivalent square-width impulse response described by a rectangle function [21] for the thermal response as well as for the antenna response of our detectors:

$$\begin{aligned} &\text{thermal response: } h_{det}(x) \equiv h_{therm}(x) = \text{rect}(x / x_{therm}) \ , \\ &\text{antenna response: } h_{det}(x) \equiv h_{ant}(x) = \text{rect}(y / x_{ant}) \ . \end{aligned} \tag{3}$$

where x_{therm} and x_{ant} represent the widths in x-direction of the thermal and antenna impulse responses of our detector. We can then describe the thermal response $V_{min}(x)$ by the function

$$V_{min}(x) = A_{1x} \int_{-x_{therm}/2}^{+x_{therm}/2} B(x-\xi)\, d\xi \ , \tag{4}$$

where A_{1x} determines the amplitude of the signal. The determination of the principal widths of the antenna spatial response is performed on the basis of the profiles $V_{max}(x)$ and $V_{max}(y)$ measured for the polarization parallel to the antenna axis. The additivity of the different contributions to the measured signal permits description of $V_{max}(x)$ as

$$V_{max}(x) = V_{min}(x) + \Delta V(x)$$
$$= A_{1x} \int_{-x_{therm}/2}^{+x_{therm}/2} B(x-\xi)\,d\xi + A_{2x} \int_{-x_{ant}/2}^{+x_{ant}/2} B(x-\xi)\,d\xi \ . \qquad (5)$$

The profiles $V_{min}(x)$ and $V_{min}(y)$ measured with our detectors are fitted with the function (4) evaluated numerically (Fig. 5). The free parameters x_{therm} and y_{therm} describe the relevant widths in the two scanning directions of the thermal impulse response of the diode. Subsequently, the profiles $V_{max}(x)$ and $V_{max}(y)$ are fitted with the aid of (5). The spatial impulse response of the antenna is determined in the two principal directions by the fitted widths x_{ant} and y_{ant}.

4. SPATIAL RESPONSE

All the sets of four scans $V_{min}(x)$, $V_{min}(y)$, $V_{max}(x)$, $V_{max}(y)$ recorded with several diodes are fitted by the appropriate function (4) or (5). The values of x_{therm}, x_{ant}, y_{therm} and y_{ant} determined by this method are then averaged over the measurements performed with diodes with similar integrated antennas. The half-widths of the rectangle impulse response functions are plotted as functions of the half arm-length L/2 of the antennas in Fig. 8. The error bars in these graphs indicate the standard deviations that characterize the reproducibility of our measurements. Our fitting procedure implies a larger variation for convolutions with rectangle functions with small widths. In addition, fitting of the V_{max} profiles with (5) includes the error associated with the characterization of the thermal response by (4). The measurements in two perpendicular directions on the effective collection area of our antenna-coupled detectors confirm that the thermal and antenna responses possess distinct collection areas (Fig. 8).

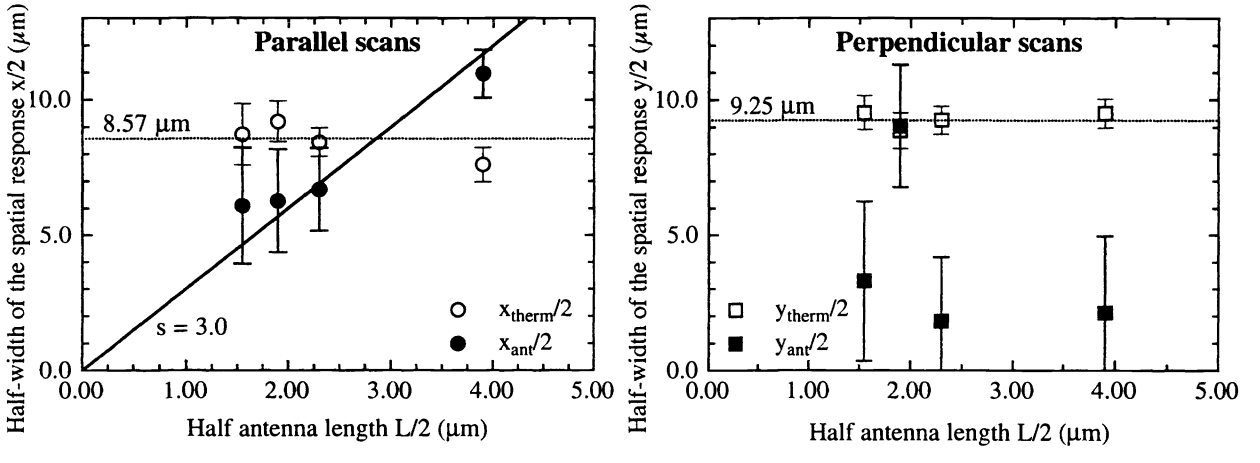

Fig. 8: Half-widths $x_{therm}/2$, $x_{ant}/2$ and $y_{therm}/2$, $y_{ant}/2$ of the impulse response of our antenna-coupled detectors versus half-antenna length L/2 for parallel scans (left-hand side) and perpendicular scans (right-hand side).

The thermal response of our detector is relatively independent on the antenna type and on the polarization of the incident radiation. The averages of all the $x_{therm}/2$ and $y_{therm}/2$ measurements are plotted as dotted lines in Fig. 8. A small asymmetry in the form of a narrowing of the thermal effective area in the scanning direction parallel to the antenna axis for the larger bow-tie antennas is likely due to a shadowing effect of the antenna. The thermal effective area of our detector is mainly determined by thermal diffusion in the substrate and therefore depends on the substrate material.

The effective receiving area for the antenna response of our detectors permits more general conclusions that can be applied to other antenna-coupled detectors. The half-width $x_{ant}/2$ in the scanning direction parallel to the antenna axis increases with increasing antenna length as shown in Fig. 8. The parallel profiles measured on our longest bow-tie antenna with L/2 = 3.9 μm are the only profiles measured that show an antenna response noticeably broader than the thermal response. The overall dependence indicates that the width of the effective receiving area parallel to the antenna axis scales with the

physical dimension of the antenna structure in this direction. The approximation of the data by a linear function is also plotted in Fig. 8.

The impulse response half-widths $y_{ant}/2$ of our antenna signals in the direction perpendicular to the antenna axis are smaller than in the direction parallel to the antenna axis, except for our shortest bow-tie antenna with a half-length $L/2 = 1.9$ µm. The polarization dependence of the signals measured with these particular devices and, consequently, the antenna response ΔV was small. In this case, we assume that the structure does not achieve a resonance at 10.6 µm wavelength. The antenna characteristic of the device is not related to the bow-tie structure. Thus, the influence of the electrical leads to the diode could explain the more extended spatial response measured in the perpendicular profiles. In addition, the polarization response of our shorter bow-tie was not maximal for the polarization parallel to the antenna axis, but for polarizations at angles of about 25°. The profiles measured in perpendicular direction for the other lengths of the antenna arm investigated in this study seem independent of the antenna shape. The half-widths $y_{ant}/2$ of the impulse responses range from $\lambda_{eff}/2$ to λ_{eff}.

The results of the profile measurements on our diodes connected to dipole antennas are schematically represented in Fig. 9. The receiving areas of the detector are approximated as ellipses. The collection ellipse associated with the thermal response of the diode possesses principal axes x_{therm} and y_{therm} and shows almost a circular symmetry. The collection area of the antenna is approximated by an ellipse with principal axes x_{ant} and y_{ant}. The axial ratio of this ellipse is $y_{ant}/x_{ant} \approx 0.54$. A theoretical calculation of the point-spread function (PSF) for an antenna-coupled detector is described in [7]. Figure 3 of this reference predicts that the principal axes of the effective collection area of the antenna-coupled detector yield a ratio $y_{ant}/x_{ant} \approx 0.5$. From our experimental data with a full-wave dipole antenna we conclude that the fringe fields past the physical dimension of the antenna are in the order of one effective wavelength λ_{eff} of the incident radiation (Fig. 9).

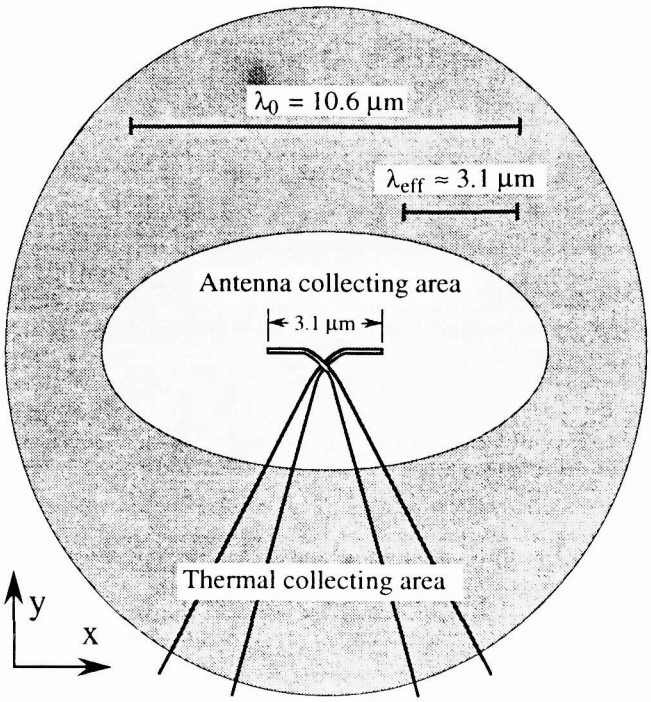

Fig. 9: Measured effective collection areas A_{coll} of a thin-film Ni-NiO-Ni detector integrated with a dipole antenna of half length $L/2 = 1.55$ µm.

5. RESPONSIVITY

A quantitative radiometric comparison in terms of the responsivities of our detectors with different antenna geometries is possible after determination of their collection area. Information on the irradiance and collection area permits a calculation of the power received.

We have performed a calculation of the responsivity of our detectors based on the data presented in [14]. In this reference, the responses of diodes with contact areas of about 140 nm × 140 nm are measured for a given irradiance E_{in} = 500 W/cm^2. The averaged signals $\overline{V_{min}}$ and $\overline{\Delta V}$ are displayed in Table 1 for our detectors with various antenna geometries. The collection areas A_{coll} of the thermal and antenna responses are approximated by the areas of ellipses with the principal axes x_{therm} and y_{therm} respectively x_{ant} and y_{ant} determined in our measurements.

The thermal responsivity R_{therm} is calculated with on the basis of the signal $\overline{V_{min}}$. Effectively it does not depend on the antenna type (Table 1). The antenna responsivities also listed in Table 1 are evaluated with the antenna signals $\overline{\Delta V}$. These antenna responsivities show a strong dependence on the antenna type. They therefore permit a comparison of our infrared antennas of different geometries despite the fact that a change of the detector area modifies the impedance-matching conditions and influences slightly the responsivity ratios between the different devices.

The best responsivities are definitely attained by the detectors connected to bow-tie antennas with the half-length L/2 = 2.3 μm. At the applied frequency of 28 THz the attenuation of the antenna currents [3] on the longest bow-tie antennas with L/2 = 3.9 μm explains their lower responsivity. The shorter bow-tie antenna with L/2 = 1.9 μm does not constitute a resonant structure at the wavelength used. This is suggested by the nontypical extent of their collection area and by the polarization behaviour of these devices. This explains their low antenna responsivity.

Antenna type	Thermal A_{coll} (μm^2)	Antenna A_{coll} (μm^2)	$\overline{V_{min}}$ (μV)	$\overline{\Delta V}$ (μV)	R_{therm} (V/W)	R_{ant} {V/W)
Dipole L/2 = 1.55 μm	261.4	63.1	125.0	119.0	0.096	0.38
Bow-tie L/2 = 1.9 μm	256.6	178.1	160.2	135.6	0.125	0.15
Bow-tie L/2 = 2.3 μm	245.2	38.0	152.2	245.8	0.124	1.29
Bow-tie L/2 = 3.9 μm	227.4	73.0	140.0	88.4	0.123	0.24

Table 1: Collection areas A_{coll}, measured signals and responsivities R of the detectors integrated with the different antennas investigated in this study. $\overline{V_{min}}$ and $\overline{\Delta V}$ represent the average of the polarization-independent and polarization-dependent contributions over a set of measurements.[14]

6. CONCLUSIONS

In summary, we have determined the effective collection area of antenna-coupled thin-film infrared detectors by measuring scans of the incident beam in two orthogonal directions. The polarization dependence of the response of our Ni-NiO-Ni detectors permits the distinction of two additive contributions originating in the rectification of antenna currents and in a thermal detection process. The spatial extent of the thermal effect was showed to be almost independent on the antenna geometry and on the scanning directions. The collection area of our infrared antennas is noticeably less extended than the area defining the thermal cross talk except for our larger antennas. In the direction parallel to the antenna axis, the width of this collection area scales with the physical length of the antenna. In the direction perpendicular to the antenna axis, we have found a receiving area with a relatively narrow width. The fringe fields surrounding the antenna in the direction parallel to the antenna axis have an extent in the order of the effective wavelength λ_{eff} of the incident radiation in the substrate. In the direction perpendicular to the antenna axis, the extent of the fringe fields can be estimated between $\lambda_{eff}/2$ and λ_{eff} on each side of the antenna axis.

Our experiments permit a better radiometric characterization and a comparison of our devices integrated with various antenna types. The most efficient detectors tested in this study were connected to bow-tie antennas with a resonant half-length L/2 = 2.3 μm. These devices exhibit the best performances represented as absolute magnitude of the signals for a given irradiance but moreover characterized as responsivity, when considering the collected power. The collection area is also a parameter of particular importance the design of focal-plane arrays. It determines the spacing of individual detectors of an array in order to minimize the cross-talk between adjacent devices.

7. ACKNOWLEDGEMENTS

The authors are greatly indebted to Prof. Dr. H. Melchior, Swiss Federal Institute of Technology (ETH) Zürich; P. Vettiger and G. Sasso, IBM Research Laboratory, Rüschlikon; Dr. F. Heiniger, Swiss Defense Procurement Agency (GR/EMD), Bern; Dr. I. Wilke, University of Hamburg, for active support and advice. This study was supported by GR/EMD, Bern; Swiss Federal Institute of Technology (ETH), Zürich; and IBM Research Laboratory, Rüschlikon. G.D. Boreman acknowledges the support of Ballistic Missile Defense Organization.

8. REFERENCES

1. J.G. Small, G.M. Elchinger, A. Javan, A. Sanchez, F.J. Bachner, D.L. Smythe, "Ac electron tunneling at infrared frequencies: Thin-film M-O-M diode structure with broad-band characteristics", Appl. Phys. Lett. **24**, pp. 275-279 (1974)
2. E. Wiesendanger, F.K. Kneubühl, "Thin-film MOM-diodes for infrared detection", Appl. Phys. **13**, pp. 343-349 (1977)
3. I. Wilke, W. Herrmann, F.K. Kneubühl, "Integrated nanostrip dipole antennas for coherent 30 THz infrared radiation", Appl. Phys. **B 58**, pp. 87-95 (1994)
4. I. Wilke, Y. Oppliger, W. Herrmann, F.K. Kneubühl, "Nanometer thin-film Ni-NiO-Ni diodes for 30 THz radiation", Appl. Phys. **A 58**, pp. 329-341 (1994)
5. C. Fumeaux, G.D. Boreman, W. Herrmann, H. Rothuizen, F.K. Kneubühl, "Polarization response of asymmetric-spiral infrared antennas", Appl. Opt. **36**, pp. 6485-6490 (1997)
6. E.N. Grossman, J.E. Sauvageau, D.G. McDonald, "Lithographic spiral antennas at short wavelengths", Appl. Phys. Lett. **59**, pp. 3225-3227 (1991)
7. G.D. Boreman, A. Dogariu, C. Christodoulou, D. Kotter, "Modulation transfer function of antenna-coupled infrared detector arrays", Appl. Opt. **35**, pp. 6110-6114 (1996)
8. E.N. Grossman, D.G. McDonald, J.E. Sauvageau, "Two-dimensional analysis of microbolometer arrays", J. Appl. Phys. **68**, pp. 5409-5414 (1990)
9. L.O. Hocker, D.R. Sokoloff, V. Daneu, A. Szoke, A. Javan, "Frequency mixing in the infrared and far-infrared using a metal-to-metal point contact diode", Appl. Phys. Lett. **12**, pp. 401-402 (1968)
10. S.Y. Wang, T. Izawa, T.K. Gustafson, "Coupling characreristics of thin-film metal-oxide-metal diodes at 10.6μm", Appl. Phys. Lett. **27**, pp. 481-483 (1975)
11. C. Fumeaux, W. Herrmann, H. Rothuizen, P. De Natale, F.K. Kneubühl, "Mixing of 30 THz laser radiation with nanometer thin-film Ni-NiO-Ni diodes and integrated bow-tie antennas", Appl. Phys. **B 63**, 135-140 (1996)
12. C. Fumeaux, W. Herrmann, F.K. Kneubühl, H. Rothuizen, B. Lipphardt, C.O. Weiss, "Mixing of 28 THz (10.7 μm) CO_2-Laser Radiation by Nanometer Thin-film Ni-NiO-Ni Diodes with Difference Frequencies up to 176 GHz", Infrared Phys. & Techn. **38**, pp. 393-396 (1997)
13. C. Fumeaux, W. Herrmann, F.K. Kneubühl, H. Rothuizen, B. Lipphardt, C.O. Weiss, "Nanometer thin-film Ni-NiO-Ni diodes for mixing 28 THz CO_2-laser emissions with difference frequencies up to 176 GHz", Appl. Phys. B **66**, in print (1998)
14. C. Fumeaux, W. Herrmann, F.K. Kneubühl, H. Rothuizen, "Nanometer Thin-film Ni-NiO-Ni Diodes for Detection and Mixing of 30 THz Radiation", Infrared Physics & Technology, in print (1998) (PhD thesis C. Fumeaux)
15. C.R. Brewitt-Taylor, D.J. Gunton, H.D. Rees, "Planar antennas on a dielectric surface", Electr. Lett. **17**, pp. 729-730 (1981)
16. G.H. Brown, O.M. Woodward, "Experimentally determined radiation characteristics of conical and triangular antennas", RCA Rev. **13**, pp. 425-452 (1952)
17. R.C. Compton, R.C. McPhedran, Z. Popovic, G.M. Rebeiz, P.P. Tong, D.B. Rutledge, "Bow-tie antennas on a dielectric half-space: Theory and experiment", IEEE Trans. AP-**35**, pp. 622-631 (1987)
18. M. Heiblum, S. Wang, J.R. Whinnery, T.K. Gustafson, "Characteristics of integrated MOM junctions at dc and at optical frequencies", IEEE J. QE-**14**, pp. 159-169 (1978)
19. E.L. Dereniak, G.D. Boreman, "Infrared detectors and systems", Chapt. 13, John Wiley & Sons, New York (1996)
20. Y Suzaki, A. Tachibana, "Measurement of the μm sized radius of Gaussian laser beam using the scanning knife-edge", Appl. Opt. **14**, pp. 2809-2810 (1975)
21. F.K. Kneubühl, "Oscillations and Waves", Springer-Verlag, Berlin (1997)